EVOLUTION OF RADIAL FORCE BALANCE AND RADIAL

TRANSPORT OVER A L-H TRANSITION

A Thesis
Presented to
The Academic Faculty

by

Min-hee Shin Sayer

In Partial Fulfillment
of the Requirements for the Degree
Master of Science in the
Nuclear and Radiological Engineering Program
School of Mechanical Engineering

Georgia Institute of Technology
December 2012

EVOLUTION OF RADIAL FORCE BALANCE AND RADIAL

TRANSPORT OVER A L-H TRANSPORT

Approved by:

Dr. Weston M. Stacey, Advisor
Nuclear & Radiological Engineering Program
School of Mechanical Engineering
Georgia Institute of Technology

Dr. Bojan Petrovic
Nuclear & Radiological Engineering Program
School of Mechanical Engineering
Georgia Institute of Technology

Dr. Dingkang Zhang
Nuclear & Radiological Engineering Program
School of Mechanical Engineering
Georgia Institute of Technology

Date Approved: 11/6/2012

I asked God for strength, that I might achieve.

I was made weak, that I might learn humbly to obey.

I asked for health, that I might do great things.

I was given infirmity, that I might do better things.

I asked for riches, that I might be happy.

I was given poverty, that I might be wise.

I asked for power, that I might have the praise of men.

I was given weakness, that I might feel the need of God.

I asked for all things, that I might enjoy life.

I was given life, that I might enjoy all things.

I got nothing I asked for but everything I hoped for.

Almost despite myself, my unspoken prayers were answered.

I am, among men, most richly blessed.

- unknown

ACKNOWLEDGEMENTS

TABLE OF CONTENTS

LIST OF TABLES

LIST OF FIGURES

SUMMARY

Understanding of plasma confinement is an essential component in development of a fusion reactor. Plasma confinement directly relates to performance of a fusion reactor in terms of energy replacement time requirements on other design parameters. Although a variety of levels of confinement have been achieved under different operating conditions in tokamaks, tokamak confinement is generally identified as being either Low (L-mode—poor confinement) or High (H-mode—good confinement). It has long been noted that radial profiles of density, temperature, rotation velocity and radial electric field are quite different for L-mode and H-mode confinement.

In operation of a tokamak experiment, the plasma confinement condition generally changes from L-mode to H-mode over a few hundred milliseconds, sometimes quite sharply. Such a difference in transition period seems to be largely due to operating conditions of the plasma. Comparison of experimental data exhibits various distinctions between confinement modes. One noteworthy distinction between confinement modes is development of steep density and temperature gradients of electrons and ions in the plasma edge region of High confinement, H-modes, relative to Low-confinement, L-modes.

The fundamental reason for the change for L-mode to H-mode is not understood. Previous studies have suggested that it is the development of reduced diffusive transport coefficients that require a steepening of the gradients in a localized region in the edge plasma, the "transport barrier" in H-mode confinement. Other studies show that the radial force balance between pressure gradient forces and electromagnetic (radial electric field and VxB) forces require radial particle fluxes to satisfy a pinch-diffusion relation that varies as these forces change. A recent study suggests that the major differences between L-mode and H-mode are associated with the electromagnetic forces in the

"pinch velocity" and the pressure gradient, not in the diffusion coefficients that multiplies the pressure gradient.

The present research examined in detail the time evolution of the radial force balance and the particle and energy transport during the L-H transition. For the analysis, DIII-D shot #118897 is selected for transition between L- and H-mode confinement. Plasma conditions in L-mode, near the L-H transition and following the transition are selected for analysis of various parameter profiles.

The initial analysis is based on the four principal equations for plasma: particle balance, momentum balance, force balance and heat conduction. Based on these equations, specific equations have been derived for: toroidal and radial momentum balances, diffusion coefficient, pinch velocity and heat conduction relation for interpretation of experimental transport parameters. The analysis of these equations, using the measured data, establishd how various terms in the radial force balance (radial electric field, VXB (electromagnetic) force, and pressure gradient) and the diffusive transport coefficients evolve over the confinement mode transition.

CHAPTER 1

BACKGROUND

1.1 Nuclear reactions and fusion

There are two methods of power generation based on nuclear energy: fission and fusion. Both methods enable the generation of large amount of energy with small amount of resources, implementing similar working principles of nuclear physics. It is not possible to obtain energy from both fission and fusion for all elements and isotopes, as most of the lightest elements will release energy by fusion and most of the heaviest elements by fissioning.

The feasibility of nuclear reaction processes for a given element is determined based on the binding energy of its atomic structure, as shown in Fig. 1.
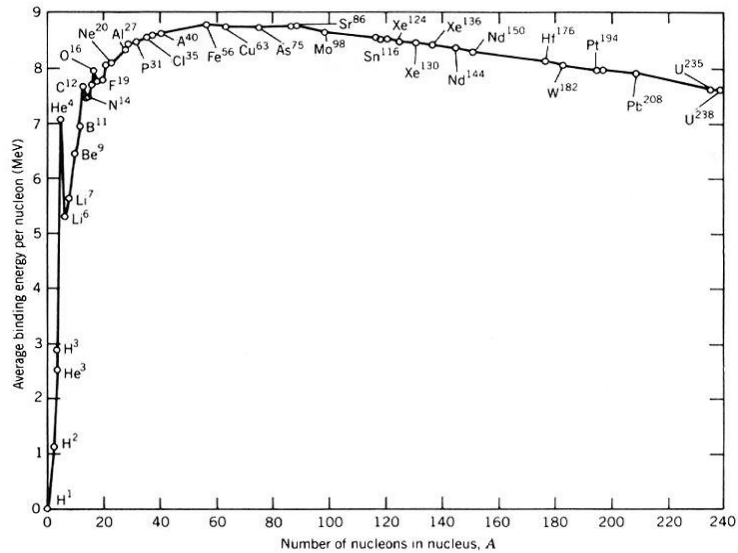

FIGURE 1: Nuclear binding energy as a function of atomic mass number[1]

Binding energy is an indicative measure of the mass defect between its nucleus and the sum of its components. It is defined as the amount of energy required to disassemble a nucleus into its components. In relation to nuclear reactions, it is the

measure of energy released for a given reaction. Based on Fig. 1, it can be determined that iron (Fe) has the highest binding energy. In general, elements lighter than iron are subject to undergo fusion and heavier elements fission[2].

General energetics determines the energy release in both fission and fusion. Nuclear power generation is based on the mass difference between the isotopes involved in the reaction, which indicates a conversion of mass to energy. The energy is released in the form of kinetic energy of recoiling nuclei and nuclear particles. For a given nuclear reaction, the mass defect is generally calculated with rest mass energy[3].

$$a+b \rightarrow (compound)^* \rightarrow c+d$$
$$\Delta m = (m_a + m_b) - (m_c + m_d)$$

(1)

The calculation of mass defect in a reaction is based on the rest mass energy of atoms, which is described by Einstein's famous equation.

$$E = m_0 c^2$$

(2)

Nuclear fusion is the process of combining two lighter isotopes to produce a heavier isotope. Fusion involves i) combination of two light nuclei, ii) formation of an unstable compound nucleus, and iii) decay into two or more nuclei and nuclear particles. In the process, the mass defect between reactants and products is converted into energy. In theory, nuclear fusion can provide unlimited amount of energy through i) a self-sustaining fuel cycle and ii) a tritium breeding method. Table 1 lists known fusion reactions and the corresponding amount of released energy[3]. Each reaction involves different combinations of reactant isotopes with varying amounts of energy released.

TABLE 1: Fusion reactions and corresponding Q-values

REACTION		Q-value
REACTANTS	PRODUCTS	(MeV)
D + T	^{4}He + n	17.6
D + D	T + p	4
	^{3}He + n	3.25
D + ^{3}He	^{4}He + p	18.2

The feasibility of fusion reactions is related to the interaction probability (also referred as cross section of reaction) as a function of energy. Interaction probabilities for given fusion reactants are shown in Fig. 2 as a function of energy. It can be determined that the deuterium-tritium reaction is the most feasible fusion reaction with the largest probability of reaction for the lowest required energy.
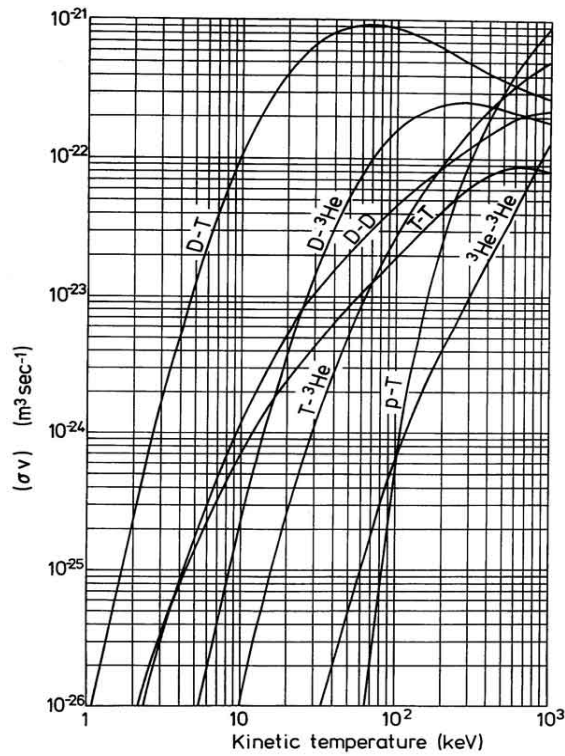
FIGURE 2: Fusion reaction rate[4]

Majority of the listed fusion reactions involve the use of hydrogen isotopes, deuterium and tritium, as reactants. Two hydrogen isotopes are easily produced or found in water. The composition of hydrogen indicates deuterium abundance of 0.0153 at.% in natural state[5]. The composition indicates that deuterium can be harvested from any water source, which presents an unlimited abundance and availability. In addition to deuterium sources, tritium can be produced through i) absorption of neutrons by lithium isotopes, as listed in table 2, and ii) the D+D reaction. In fusion reactor designs, lithium isotopes are

contained in the blanket in order to breed tritium. Neutron absorption reactions for tritium breeding are listed in table 2.

TABLE 2: Tritium breeding reactions[6]

REACTION	
REACTANTS	PRODUCTS
$n+^6Li$	$T+^4He$
$n+^7Li$	$T+^4He+n'$

1.2 Plasma

Plasma is often known as the forth state of matter alongside solid, liquid, and gas. It displays distinctive characteristics as a phase of material that differs from other phases. Plasma is defined as a collection of atomic particles free of coulombic and nuclear bonding[3], e.g. free ions and electrons. In such a state, particles interact in two different methods. Electrons, neutrons and protons that compose an atom are able to interact with nearby particles. Charged particles interact via coulombic interaction and scattering and neutrons via scattering.

For the purpose of power generation based on fusion, a thermonuclear plasma state is required to generate sufficient amount of power. A thermonuclear plasma is defined as plasma heated to an extremely high temperatures, on the order of 10^7 K.

1.3 Magnetic confinement and tokamak

In today's fusion research, the leading confinement concept is magnetic confinement. The concept is based on the Lorentz force on moving charged particles in a magnetic field, which is orthogonal to both the particle velocity and the magnetic field. The magnetic confinement operates based on the utilization of electromagnets surrounding a plasma chamber. Electromagnets produce magnetic fields that apply

forces on plasma ions and electrons as a confinement method. The leading magnetic

confinement concept, the tokamak, was first introduced by Soviet Union scientists who

developed the concept of a toroidal chamber with a set of coils surrounding it. As shown

in Fig. 2, tokamak devices are composed of a plasma confinement chamber and

surrounding toroidal and poloidal coils. In addition, leading tokamak devices feature

various plasma heating methods, external fueling sources and a surrounding vaccum

chamber for an improvement in the performance of the device. The tokamak is

considered the most feasible method of plasma confinement for power generation. The

leading tokamak design of the International Thermonuclear Experimental Reactor (ITER)

includes 18 toroidal and 6 poloidal superconducting coils for magnetic field generation, a

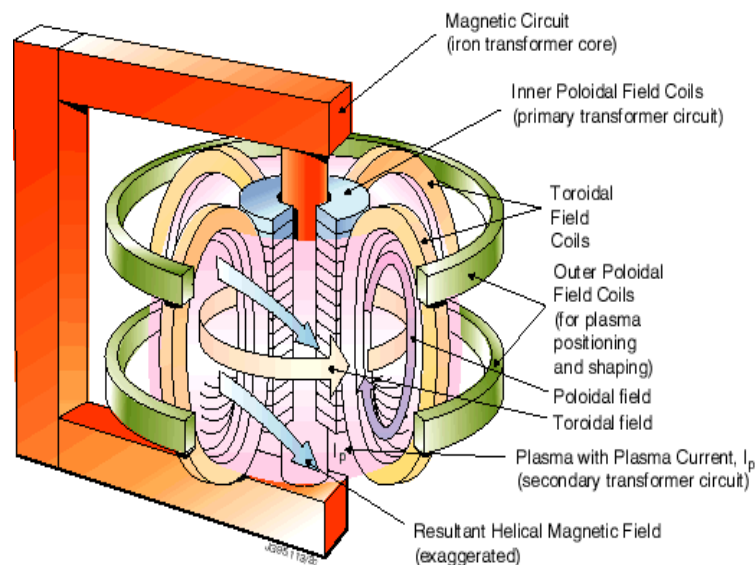helium-cooled vacuum chamber, and various external heading devices[7].

FIGURE 3: Tokamak reactor[8]

1.4 Importance of confinement

Plasma confinement determines two major factors in the development of a fusion

reactor: i) the feasibility of fusion reactor operation and ii) plasma performance. The

feasibility of fusion reactor operation depends heavily on plasma confinement. Several factors are considered for the feasibility of fusion such as plasma temperature and power balance. In terms of power balance, plasma energy and energy loss are considered as shown in Eq. 3.

$$\frac{1}{4}n^2 \langle \sigma \upsilon \rangle_{fus} U_\alpha \left(1 + \frac{5}{Q_p} \right) \geq f_z n^2 L_z + \frac{3nT}{\tau_E} \qquad (3)$$

The plasma power balance equation accounts for the sum of external and plasma heating power on the left side and radiation and transport loss on the right. n is the total density, $\langle \sigma \upsilon \rangle_{fus}$ is the fusion reactivity, U_α is the alpha particle energy in fusion, f_z and L_z are the ion fraction and radiation emissivity of the plasma, T is the plasma temperature, and τ_E is the energy confinement time. Q_p in power balance equation is the plasma amplification factor, a measure of fusion feasibility. The plasma energy amplification factor is calculated as the ratio of fusion power and external heating input power, as shown in Eq. 4.

$$Q_p = \frac{P_{fusion}}{P_{ext.heating}} \qquad (4)$$

Another measure of fusion feasibility is the Lawson criterion of ignition, shown in Eq.5. The expression is derived from the plasma power balance equation by neglecting the radiation loss term.

$$nT\tau_E \geq \frac{12}{const \times U_\alpha} \equiv \left(nT\tau_E \right)_{Lawson} \qquad (5)$$

The progress of fusion reactor performance is determined based on two parameters, the Lawson criterion of ignition and the plasma amplification factor. Current research reactors with D-D and D-T fuels have not reached commercial reactor confinement modes[6].
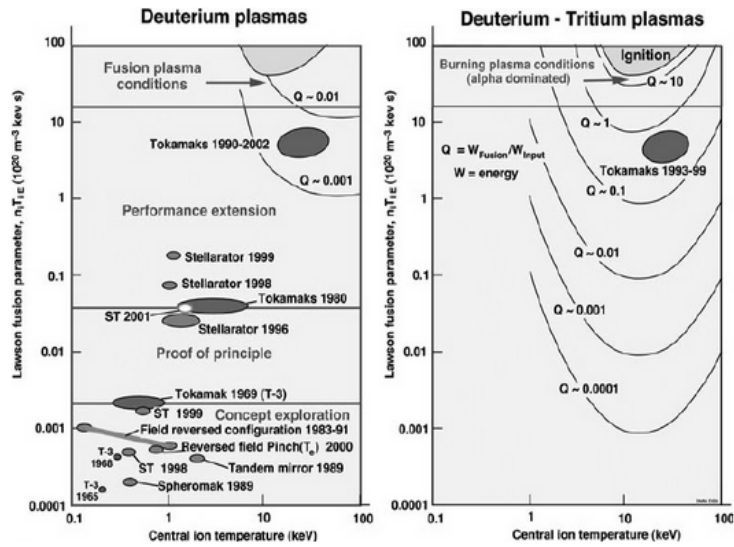
FIGURE 4: Lawson criterion and power amplification factor for plasma type[6]

The importance of confinement quality is directly related to the calculation of feasibility parameters, the Lawson criterion and the plasma energy amplification factor. The energy confinement time appears directly in the calculation of the Lawson criterion. An increase in the energy confinement time directly indicates the improvement in confinement quality. Experimental surveys have determined that plasma confinement improvement leads to a great increase in temperature and density. Results indicate that an improvement in plasma confinement generate a higher Lawson criterion of ignition. In P_{fusion} for the plasma amplification factor, temperature and density play important roles in determining fusion power. The energy of the plasma is directly related to the increase in temperatures and densities that arise as a result of confinement improvement.

CHAPTER 2

INTRODUCTION

With the first achievement of higher quality plasma confinement[9] (H-mode), analysis of the differences between low (L-mode) and high confinement (H-mode) regimes[10] and the transition between them emerged as a major focus of tokamak research that continues today[11].   Analysis of the L-mode to H-mode transition has led to identification of distinctions in plasma profiles associated with confinement mode changes[10]. One distinction involves a drastic change in radial electron density and temperature profiles. In L-mode, density and temperature profiles decrease only gradually as a function of increasing radius within the edge plasma. However, when the plasma transitions from L-mode to H-mode, a sharp steepening of the gradient is displayed in both the density and temperature profiles across the edge region, which is referred to as the formation of an edge pedestal. In general, the edge pedestal appears just inside the LCFS (last closed flux surface) at normalized radius greater than 0.86. Other distinctions between L-mode and H-mode regimes includes changes in the radial electric field and rotational velocity profiles in the edge plasma[10,12].

The study of the physics of the edge pedestal has been a major research area for decades because of its importance for the performance of future tokamaks such as the International Thermonuclear Experimental Reactor (ITER)[13]. Based on previous studies[13,14], researchers have determined that the performance of ITER may depend heavily on the temperature and density of the edge pedestal, hence on the temperature and density gradients in the edge pedestal.

The causes of the transition of the edge pedestal profiles from the L-mode to H-mode forms remain a subject of active theoretical and experimental investigation (as summarized recently in Ref. 11).   The formation of a "transport barrier" due to the shear

suppression of fluctuation-driven diffusive transport coefficients[15,16], the penetration and ionization of recycling neutrals[17], pressure gradient limits set by microinstabilities[18] and non-diffusive transport[19,20] associated with electromagnetic forces and ion orbit loss have been investigated.

This paper reports an interpretation of the detailed time evolution of measured density, temperature and rotation profiles across the L-H transition in terms of non-diffusive as well as diffusive transport mechanisms; i.e. the evolution of the electromagnetic forces, pressure gradients, rotation velocities and momentum transport frequencies (which determine the particle diffusion coefficient), thermal diffusion coefficients and ion orbit loss during an L-H transition in a DIII-D discharge[21]. Density, temperature and rotation velocity profiles were resolved on roughly 50 ms intervals from just before until well after the L-H transition. The radial and toroidal force balances, the continuity equation and the energy balance equations were employed to interpret from the measured profile evolution the evolution of momentum transport rates and the particle diffusion coefficient, of the pinch velocity and of the thermal diffusivity.

CHAPTER 3

EXPERIMENTAL DATA

3.1 Discharge selection and profile fitting procedure

In order to interpret the evolution of diffusive and non-diffusive transport, DIII-D discharge #118897 was selected for the time intervals from 1525 ms (just before L-H transition) to 2140 ms (well after the L-H transition). The motivations behind selection of #118897 for analysis are i) clear and long transition between L-mode to H-mode based on the density profile at the pedestal, ii) good Magnetohydrodynamic (MHD) stability based on triangularity values, and iii) a long initial H-mode phase without ELM interruption[22]. In total, 14 time slices were selected for analysis. Selected timeslices include L-mode (1525ms), early transition (1555ms), transition (1640 - 2040ms) and fully established H-mode (2090-2140ms). These descriptions were chosen based on the electron density profile at the pedestal.

In order to construct plasma property profiles, time bins relevant to the investigation of L-H transition are selected. Each time bin contains a sufficient number of Thomson pulses and Charge Exchange Recombination (CER) spectroscopy data points to ensure the quality of data[23,24,25,26]. Experimentally obtained data includes electron density, electron temperature, ion temperature, electron pressure, carbon impurity fraction, carbon toroidal velocity and carbon poloidal velocity.

Hyperbolic tangent fits of the data points generated with Eqs. 6 and 7 were utilized for the electron properties,

$$Y = A \tanh\left(\frac{2\left(x_{sym} - x\right)}{width}\right) + B \quad \text{for } x \geq x_{knee} \tag{6}$$

$$Y = A \tanh\left(\frac{2\left(x_{sym} - x\right)}{width}\right) + B - slope \times \left(x_{knee} - x\right) \quad \text{for } x < x_{knee} \tag{7}$$

and spline fits were used for the other quantities, where parameters are obtained from fitted profiles[27]. Iterative spline fitting processes were employed to ensure an accurate representation of plasma properties. Fitted profiles were used in the GTEDGE simulation as input parameters. The experiment data measurements, analysis, and validation were performed by other members of the DIII-D team.

3.2 Experimental data

Experimental electron density and temperature profiles are shown in Figs. 5 and 6. Electron density and temperature profiles display similarity in L-H transition behavior in development of pedestal structure, an appearance of an edge pedestal structure as the plasma shifts from L-mode to H-mode. It is noted that starting at about 1640ms the edge pedestal position stays relatively fixed for both electron density and temperature profiles[27]. A general trend is observed where the electron density and temperature at the inner most radius ($\rho = 0.86$) steadily increases through transition, indicating improvement in confinement and performance
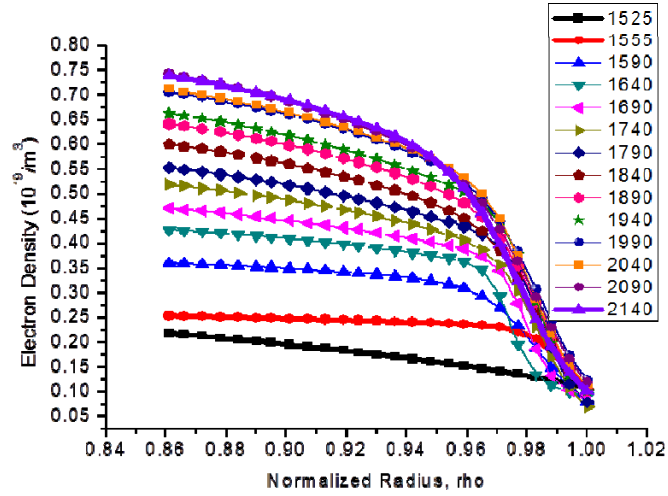
FIGURE 5: Experimental electron density profiles
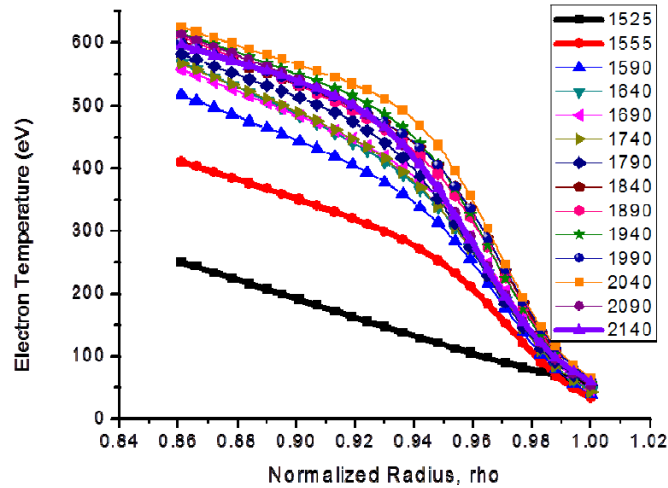
FIGURE 6: Experimental electron temperature profiles

Experimental ion temperature profiles are shown in Fig. 7. Ion temperature profiles were constructed using the spline fitting method. Ion temperature profiles, unlike electron density and temperature profiles, do not develop such a distinctive edge pedestal (sharp gradient region). Given such a characteristic in profile evolution, spline fitting method provides more accurate representation of experimental data than hyperbolic tangent method[27]. A general trend of steady increase in ion temperature at the innermost

radius ($\rho = 0.86$) is observed through the L-H transition. Just inside the separatrix ($\rho = 1$) the temperature magnitude remains at about the initial L-mode value. The ion temperature gradient in the edge pedestal initially increases at the L-H transition and then remains relatively fixed while the entire profile increases. The ion temperature profiles do not increase monotonically, but rather "oscillates" slightly; the peak temperature at the innermost mesh point ($\rho = 0.862$) is achieved at 1940ms and then decrease slightly. The major change in temperature is observed early in the transition where ion the temperature increases dramatically from 1525ms to 1590ms.
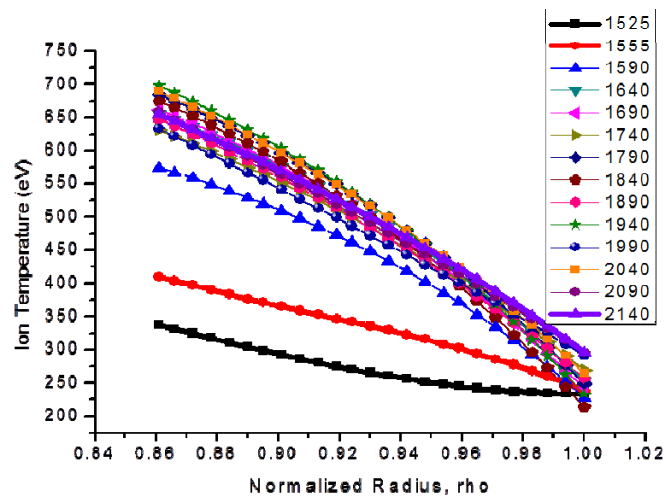
FIGURE 7: Fitted experimental ion temperature profiles

For the rotational velocity profiles, single tangential measurements are obtained and decomposed into two components: toroidal and poloidal rotation. Both rotation velocities are measured for C^{+6} impurity particles but not for the main ion particles due to weak charge-exchange associated with deuterium ions in comparison to C^{+6} ions.

Toroidal rotation velocity at the innermost radius ($\rho = 0.86$) increases steadily as the plasma undergoes the L-H transition and enters H-mode. In L-mode (1525ms), the toroidal rotataion profile is relatively flat across the edge region.

As plasma enters the transition (1555ms), a significant change occurs in the toroidal rotation velocity profile. While the rotation velocity increases at the L-H transition for ($\rho < 0.95$), a large region of decreased rotation velocity develops in the edge ($0.96 < \rho < 1.0$). This well-like structure in the toroidal rotation profiles persists to about 1740 ms, even though the magnitude of the rotation velocity generally increases at all normalized radii after 1555ms.
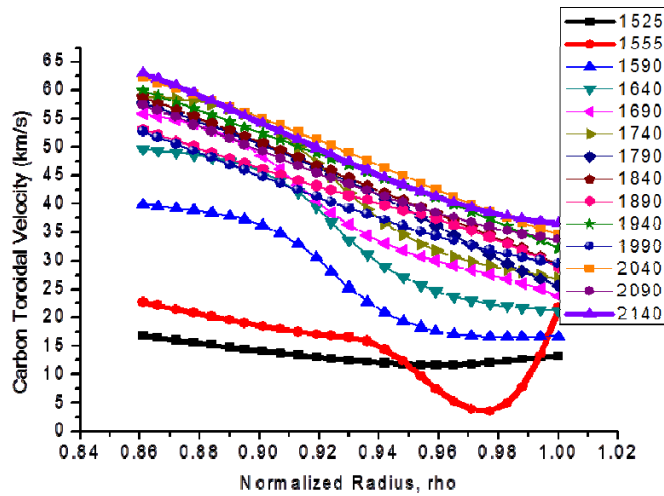
FIGURE 8: Experimental carbon toroidal rotation velocity

The evolution of the poloidal rotation velocity profiles, as shown in figure 9, displays more distinctive changes than the toroidal rotation during the L-H transition. In L-mode, the poloidal rotation velocity profile generally increases with radius, but not monotonically, exhibit a slight dip centered about $\rho = 0.97$. However, there is a sharp change in the rotation profile between 1525ms (L-mode) and 1590ms, which is not yet complete at 1555ms, changes the direction of the poloidal rotation and creates a broad negative dip centered about $\rho = 0.96$ which persists. The poloidal rotation inside of $\rho = 0.90$ becomes more positive immediately after the L-H transition (1555ms) but then becomes more negative at later times.

14

FIGURE 9: Carbon poloidal rotation velocity

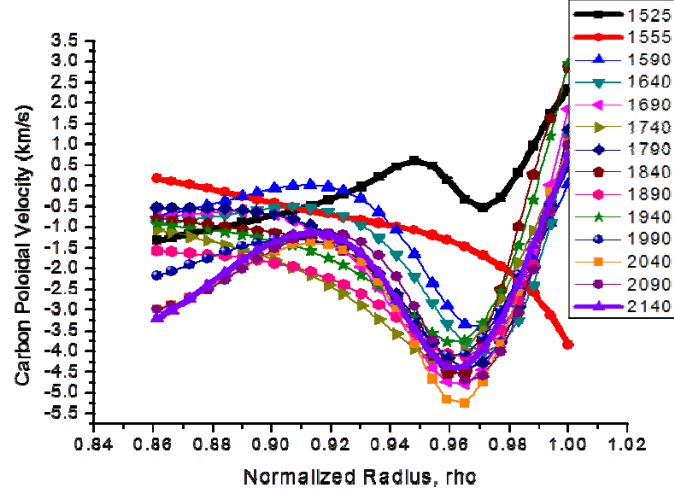## 3.3 Experimentally inferred data

The radial electric field is a calculated quantity constructed from the measured carbon impurity density, temperature and rotation velocities using the radial force balance equation

$$E_r = \frac{1}{n_i Z_i e} \nabla_r P_i - \left(V_i \times B \right)_r \qquad (8)$$

The radial electric field profile shown in Fig. 10 evolves in a similar manner to the carbon poloidal rotation velocity profile shown in Fig. 9. In L-mode (1525ms), the radial electric field profile is relatively flat across the edge region. The profile changes rather swiftly after the L-H transition as plasma enters the H-mode. Early in the transition (1555ms), the radial electric field develops a negative well-like structure reported in previous studies[10,28]. This structure is sustained throughout the transition and into the fully developed H-mode.
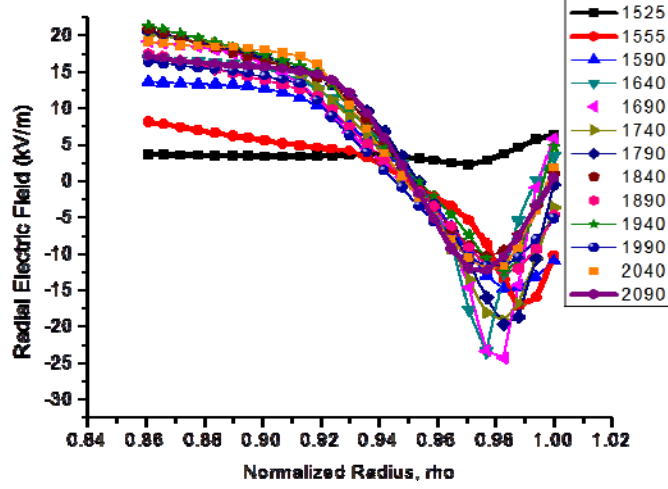
15

FIGURE 10: Radial electric field calculated from radial momentum balance on carbon.

Poloidal and toroidal rotation velocities of deuterium are inferred based on experimental and calculated parameters. The deuterium toroidal rotation velocity is inferred from the impurity toroidal rotation velocity, $V_{\phi k}$, using carbon and deuterium toroidal velocity equation and the first order perturbation theory. The perturbation estimate for difference in toroidal rotation velocities is

$$(V_{\phi j} - V_{\phi k})_0 = \frac{\left(n_j e_j E_\phi^A + e_j B_\theta \Gamma_j + M_{\phi j}\right) - n_j m_j \nu_{dj} V_{\phi k}^{\exp}}{n_j m_j \left(\nu_{jk} + \nu_{dj}\right)} \tag{9}$$

where ν_{dj} and ν_{dk} are experimental toroidal angular momentum transfer frequency for deuterium and impurity ions respectively. Momentum transfer frequencies for deuterium and carbon are calculated as part of the perturbation analysis, based on experimental parameters,

$$\nu_{dj} = \frac{\left(n_j e_j E_\phi^A + e_j B_\theta \Gamma_j + M_{\phi j}\right) + \left(n_k e_k E_\phi^A + e_k B_\theta \Gamma_k + M_{\phi k}\right)}{\left(n_j m_j + n_k m_k\right) V_{\phi k}^{\exp}} \tag{10}$$

$$\nu_{dk} = \frac{\left(n_k e_k E_\phi^A + e_k B_\theta \Gamma_k + M_{\phi k}\right) + n_j m_j \nu_{jk} (V_{\phi j} - V_{\phi k})_0}{n_k m_k V_{\phi k}^{\exp}} \tag{11}$$

16

Based on these parameters, the deuterium toroidal rotation velocity is calculated from

$$V_{\phi j}^{\exp} = V_{\phi k}^{\exp} + (V_{\phi j} - V_{\phi k})_0 = V_{\phi k}^{\exp} + \frac{\left(n_j e_j E_\phi^A + e_j B_\theta \Gamma_j + M_{\phi j}\right) - n_j m_j \nu_{dj} V_{\phi k}^{\exp}}{n_j m_j \left(\nu_{jk} + \nu_{dj}\right)} \quad (12)$$

FIGURE 11: Calculated deuterium toroidal rotation velocity profiles
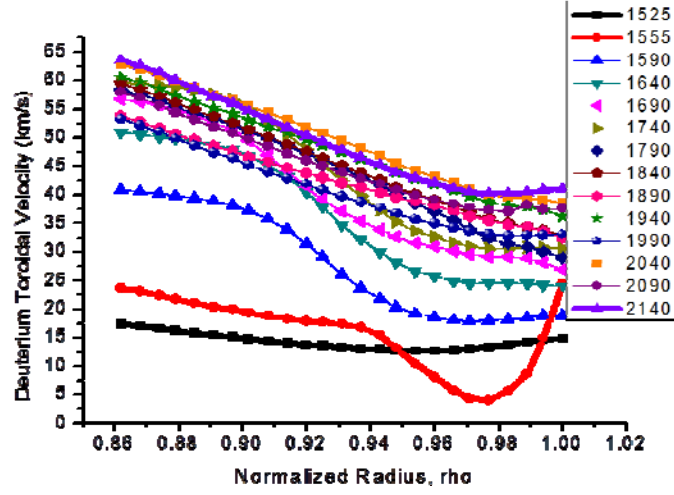
The deuterium poloidal rotation velocity is calculated using the above deuterium toroidal rotation velocity and the radial momentum balance equation for deuterium

$$V_{\theta j}^{\exp} = -\frac{E_r^{\exp}}{B_\phi} + \frac{B_\theta}{B_\phi} V_{\phi j}^{\exp} + \frac{1}{n_j e B_\theta} \frac{\partial p_j}{\partial r} \quad (13)$$

The results are shown in Fig. 12
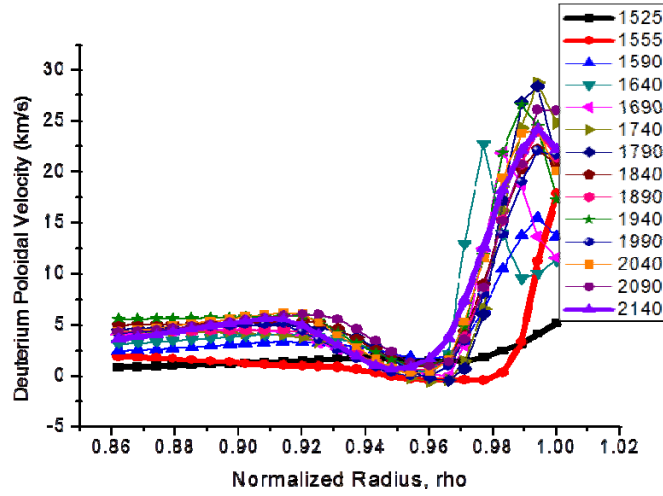
FIGURE 12: Calculated deuterium poloidal rotation velocity profiles

The deuterium and impurity ions exhibit similar toroidal rotation velocity profiles. A large negative well-like structure is observed immediately after the L-H transition (1555ms - 1640ms). Eventually, such structure disappears and relatively linear rotation velocity profiles are observed for both ion species in later stages of the H-mode regime.

For poloidal rotation velocity, very different profile evolutions are observed for the two ion species. For deuterium, a relatively flat rotation velocity profile is observed in L-mode (1525ms). This profile quickly changes with the development of slight dip around $\rho = 0.96$ and a large increase in magnitude of the positive rotation velocity for $\rho > 0.96$. The carbon poloidal rotation velocity has a more structured profile in L-mode, and develops a large negative well in the rotation velocity profile for $\rho > 0.96$.

CHAPTER 4

TRANSPORT INTERPRETATION OF EXPERIMENTAL DATA

4.1 Modeling the background plasma with GTEDGE

The background plasma is modeled with the GTEDGE code[29,30,31] which solves coupled i) power and particle balances on the core plasma to obtain particle and power fluxes into the scrap off layer (SOL) which are input to ii) "2-pt" integral power, particle and momentum balances to calculate power and particle fluxes to the divertor plate and recycling neutral fluxes from the divertor plate which are input to iii) a 2D neutral transport code that calculates charge exchange neutral fluxes to the wall and recycling neutral fluxes to refuel the core plasma. Geometric parameters such as X-point and divertor strike point locations, plasma minor and major radii and elongation are taken from experiment, as are plasma parameters such as the magnetic field, current, etc. The elongated plasma is modeled as a circular plasma with effective minor radius $\hat{r} = r\sqrt{(1+\kappa^2)/2}$ chosen to conserve (in the elliptical approximation) the flux surface area of the elongated plasma with elongation, κ. Other model parameters are adjusted so that the code predicts experimental i) line average density, ii) energy confinement time, iii) central, edge pedestal and separatrix densities and temperatures, and iv) certain other parameters. This GTEDGE background plasma calculation provides the values of particle and heat fluxes crossing the separatrix outward into the SOL and of neutral particle fluxes crossing the separatrix inward to fuel the core plasma, as well as the distribution of neutral particles in the edge plasma.

Using the input experimental density and temperature profile data, the GTEDGE code then solves the ion particle continuity equation

$$\frac{\partial (n_j V_{rj})}{\partial r} = -\frac{\partial n_j}{\partial t} + n_e n_o \langle \sigma \upsilon \rangle_{ion} + S_{nb} \qquad (14)$$

for the ion radial particle flux, $\Gamma_j(r) = n_j V_{rj}$, where the second term on the right is the ionization of recycling neutrals and the last term is the neutral beam source.
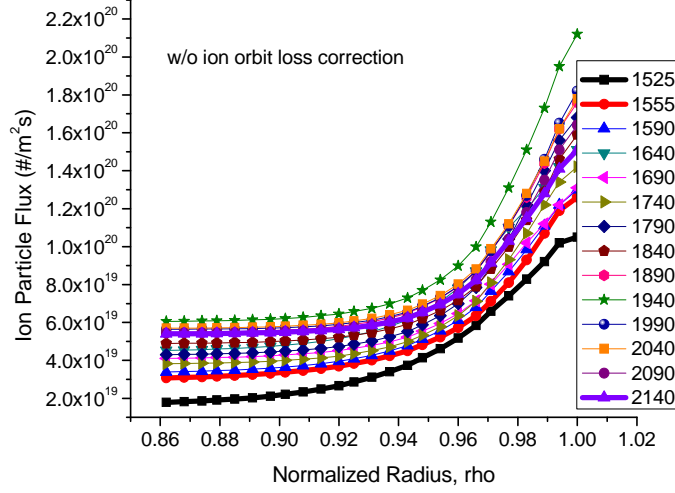

FIGURE 13: Ion particle flux

The calculated radial particle flux generally increased with radius in the edge due to the ionization of recycling neutrals, for all times analyzed between 1525 and 2140 ms. The magnitude of the calculated particle flux at all radii increased monotonically in time from 1525 ms (L-mode) until 1940 ms, then decreased monotonically in time until reaching a value about half-way between the 1525 and 1940 magnitudes at 2140ms.

The GTEDGE code also uses the input experimental density and temperature data to solve the ion and electron power balance equations

$$\frac{\partial Q_j}{\partial r} \equiv \frac{\partial}{\partial r}\left(q_j + \frac{3}{2}\Gamma_j T_j\right) = -\frac{\partial}{\partial t}\left(\frac{3}{2}n_j T_j\right) + q_{nbj} - q_{je} - n_e n_o^c \langle \sigma\upsilon \rangle_{cx} \frac{3}{2}\left(T_j - T_o^c\right) \quad (15)$$

and

$$\frac{\partial Q_e}{\partial r} \equiv \frac{\partial}{\partial r}\left(q_e + \frac{3}{2}\Gamma_e T_e\right) = -\frac{\partial}{\partial t}\left(\frac{3}{2}n_e T_e\right) + q_{nbe} + q_{je} - n_e n_k L_k(T_e) \qquad (16)$$

for the total heat fluxes of ions and electrons, $Q_i(r)$ and $Q_e(r)$, respectively.
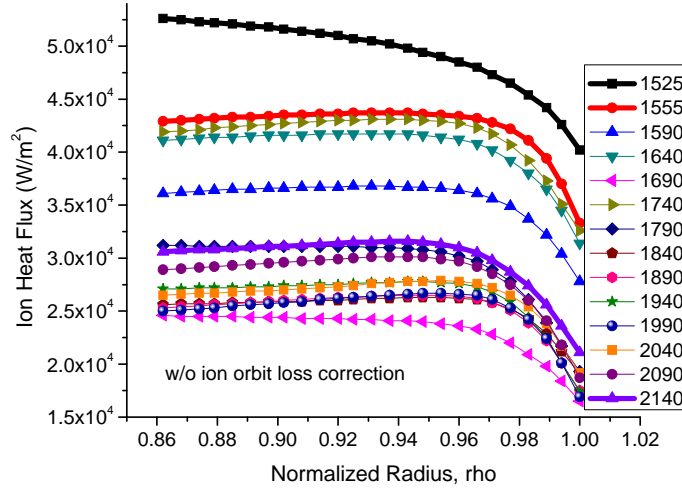
FIGURE 14: Ion heat flux
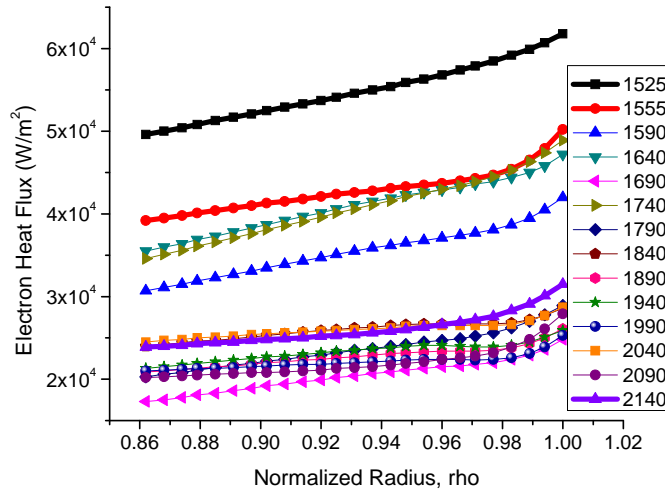
FIGURE 15: Electron heat flux

The total ion heat flux profile generally decreases with radius at all times considered due to energy exchange with the cooler electrons, with a sharp decrease just inside the separatrix due to charge-exchange cooling from interactions with recycling neutrals. There is initially a monotonic decrease of the ion heat flux prosssfile with time, but after 1590ms the change in ion profile with time become erratic. The lowest

21

magnitude ion flux profile occurs at 1690ms and is about half the magnitude of the L-mode profile at 1525ms, and the magnitude of the profile at the final time analyzed (2140ms) is about 25% larger than this lowest value.

The total electron heat flux profile generally increases with radius at all times, due to energy exchange with the hotter ions. The magnitude of the electron heat flux profiles exhibits the same variation with time as discussed above for the total ion flux profile, indicating a variation in the total energy flux into the edge region from the core plasma, not a variation in the interaction among ions and electrons in the edge plasma. The particle and heat fluxes calculated from the GTEDGE background plasma calculation described in the previous paragraph are used as separatrix boundary conditions. The q_{nb} terms represent neutral beam (or other) heating, q_{je} is the ion-to-electron collisional energy transfer, and the last terms in Eqs. 15 and 16 represent charge-exchange cooling of the ions and radiation cooling of the electrons, respectively, which are evaluated using the neutral distribution calculated as part of the background plasma calculation described in the previous paragraph. The quantities $q_{j,e}$ are the conductive heat fluxes of ions and electrons. Similar equations obtain for other ion species "k" present in the plasma, and the electron density is constrained by quasi-neutrality.

Equations 14 - 16 are particle and energy balances which determine the total outward fluxes of particles and energy. For the most part, these fluxes are due to transport processes taking place in the plasma, which we would like to interpret from the measured density, temperature and rotation profiles. However, some part of these fluxes are due to ions which free-stream out of the plasma on loss orbits that intersect with a material surface or cause the ion to be lost by scattering or charge-exchanging outside the last closed flux surface, and the above fluxes need to be reduced by the fraction of the plasma ion particle and energy fluxes due to ion orbit loss.

Following[32], we make use of the conservation of canonical toroidal angular momentum

$$RmV_{\parallel}f_{\varphi} + e\psi = const = R_0 mV_{\parallel 0}f_{\varphi 0} + e\psi_0 \qquad (17)$$

to write the orbit constraint for an ion introduced at a location "0" on flux surface ψ_0 with parallel velocity $V_{\parallel 0}$, where $f_{\varphi} = |B_{\varphi}/B|$, R is the major radius and ψ is the flux surface value. The conservation of energy and of poloidal angular momentum

$$\frac{1}{2}m(V_{\parallel}^2 + V_{\perp}^2) + e\phi = const = \frac{1}{2}m(V_{\parallel 0}^2 + V_{\perp 0}^2) + e\phi_0 \equiv \frac{1}{2}mV_0^2 + e\phi_0$$

$$\frac{mV_{\perp}^2}{2B} = const = \frac{mV_{\perp 0}^2}{2B_0} \qquad (18)$$

further require

$$V_{\parallel} = \pm V_0 \left[1 - \left|\frac{B}{B_0}\right|(1 - \zeta_0^2) + \frac{2e}{mV_0^2}(\phi - \phi_0) \right]^{\frac{1}{2}} \qquad (19)$$

where ϕ is the electrostatic potential. The quantity $\zeta_0 = V_{\parallel 0}/V_0$ is the cosine of the initial guiding center velocity relative to the toroidal magnetic field direction. Using Eq. 19 in Eq. 17 and squaring leads to a quadratic equation in the initial ion velocity $V_0 = \sqrt{V_{\parallel 0}^2 + V_{\perp 0}^2}$

$$V_0^2 \left[\left(\left|\frac{B}{B_0}\right|\frac{f_{\varphi 0}}{f_{\varphi}}\zeta_0\right)^2 - 1 + (1 - \zeta_0^2)\left|\frac{B}{B_0}\right| \right] + V_0 \left[\frac{2e(\psi_o - \psi)}{Rmf_{\varphi}}\left(\left|\frac{B}{B_0}\right|\frac{f_{\varphi 0}}{f_{\varphi}}\zeta_0\right) \right] +$$

$$\left[\left(\frac{e(\psi_0 - \psi)}{Rmf_{\varphi}}\right)^2 - \frac{2e(\phi_0 - \phi)}{m} \right] = 0 \qquad (20)$$

Note that Eq. 20 is quite general with respect to flux surface geometry representation of R, B and the flux surfaces ψ. By specifying an initial "0" location for an ion with initial direction cosine ζ_0, and specifying a final location on the flux surface ψ, Eq. 20

can be solved for the minimum initial ion speed V_0 that is required in order for the ion orbit to reach the final location.

Thus, Eq. 20 can be solved for the minimum ion energy necessary for an ion located on an internal flux surface to cross the last closed flux surface at a given location or to strike the chamber wall at a given location, etc. All of the particles with speeds greater than this $V_{0\min}(\zeta_0)$ are lost across the last closed flux surface (and assumed in this work not to return) or strike the chamber wall. For the usual DIII-D anti-parallel current/magneitic field configuration, the quantity $V_{0\min}(\zeta_0)$ is very large for particles with parallel velocity components opposite to the direction of the toroidal magnetic field $(\zeta_0 < 0)$, which execute banana orbits inside the flux surface, but becomes smaller with increasing $\zeta_0 > 0$ (i.e. as the particle velocity becomes more nearly aligned with the toroidal magnetic field direction).

GTEDGE calculates $V_{0\min}(\zeta_0)$, using the electrostatic potential calculated by integrating the input experimental radial electric field, an approximate representation of the magnetic flux surface geometry described

by $\left[R(r,\theta) = \overline{R}h(r,\theta),\, B_{\theta,\varphi}(r,\theta) = \overline{B}_{\theta,\varphi}/h(r,\theta),\, h(r,\theta) = \left(1 + (r/\overline{R})\cos\theta\right) \right]$, and an

approximate flux surface $\psi(\rho) = RA_{\varphi} = \dfrac{1}{2}\left(\dfrac{\mu_0 I}{2\pi a^2}\right)\overline{Ra}^{-2}\rho^2$ which follows from

Ampere's law and the assumption of uniform current density.

Since $V_{0\min}(\zeta_0)$ decreases with radius, cumulative (with increasing radius) particle, momentum and energy loss fractions can be defined

$$F_{orb} \equiv \frac{N_{loss}}{N_{tot}} = \frac{\int_{-1}^{1}\left[\int_{V_{0\min(\zeta_0)}}^{\infty} V_0^2 f(V_0)dV_0\right]d\zeta_0}{2\int_0^{\infty}V_0^2 f(V_0)dV_0} = \frac{\int_{-1}^{1}\Gamma\left(\frac{3}{2},\varepsilon_{\min(\zeta_0)}\right)d\zeta_0}{2\Gamma\left(\frac{3}{2}\right)} \tag{21}$$

24

$$M_{orb} \equiv \frac{M_{loss}}{M_{tot}} = \frac{\int_{-1}^{1}\left[\int_{V_{0\min(\zeta_0)}}^{\infty}(mV_0\zeta_0)V_0^2 f(V_0)dV_0\right]d\zeta_0}{2\int_0^{\infty}(mV_0)V_0^2 f(V_0)dV_0} = \frac{\int_{-1}^{1}\Gamma\left(2,\varepsilon_{\min(\zeta_0)}\right)d\zeta_0}{2\Gamma(2)} \tag{22}$$

and

$$E_{orb} \equiv \frac{E_{loss}}{E_{total}} = \frac{\int_{-1}^{1}\left[\int_{V_{0min}(\zeta_0)}^{\infty}\left(\frac{1}{2}mV_0^2\right)V_0^2 f(V_0)dV_0\right]d\zeta_0}{\int_{-1}^{1}\left[\int_0^{\infty}\left(\frac{1}{2}mV_0^2\right)V_0^2 f(V_0)dV_0\right]d\zeta_0} = \frac{\int_{-1}^{1}\Gamma\left(\frac{5}{2},\varepsilon_{\min(\zeta_0)}\right)d\zeta_0}{2\Gamma\left(\frac{5}{2}\right)} \tag{23}$$

where $\varepsilon_{\min}\left(\zeta_0\right) = mV_{0\min}^2\left(\zeta_0\right)/2kT$ is the reduced energy corresponding to the minimum velocity for which ion orbit loss is possible, and an initially Maxwellian ion distribution has been assumed. The quantities $\Gamma(n)$ and $\Gamma(n,x)$ in Eqs. 21 - 23 are the gamma function and incomplete gamma function. The ion orbit loss corrected ion particle and energy transport fluxes are then $\widehat{\Gamma}(r) = \Gamma(r)(1 - F_{orb}(r)), \widehat{Q}(r) = Q(r)(1 - F_{orb}(r))$.

The particle and energy ion loss fractions given by Eqs. 21 and 23 are shown in Figs. 16 and 17. The ion orbit loss fractions from inner flux surfaces increase after the L-H transition (>1525 ms) because the increase in ion temperature enables a larger fraction of the ion distribution to access loss orbits.
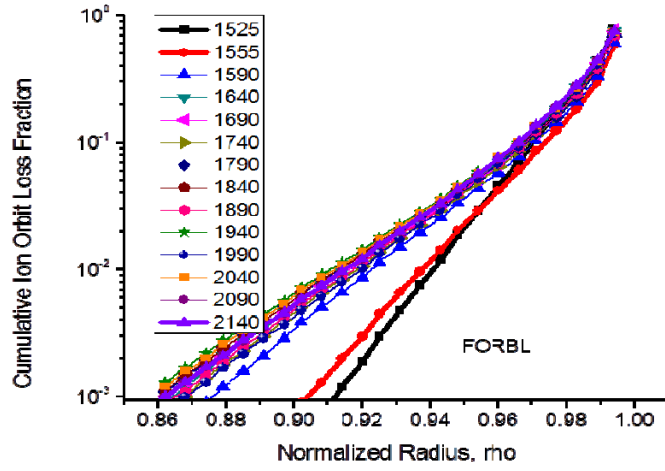
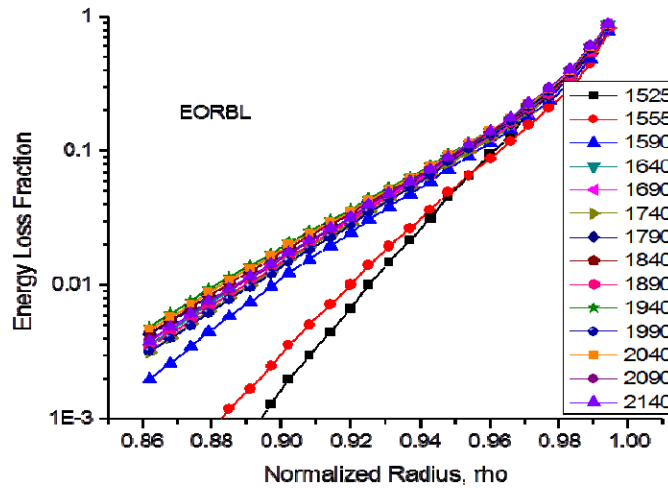FIGURE 16: Particle ion orbit loss fractions

FIGURE 17: Energy ion orbit loss fractions

The effect of these ion orbit loss fractions on the "transport" fluxes is largest just inside the separatrix, where it significantly reduces the $\hat{\Gamma}$ and $\hat{Q}$ relative to Γ and Q, respectively.
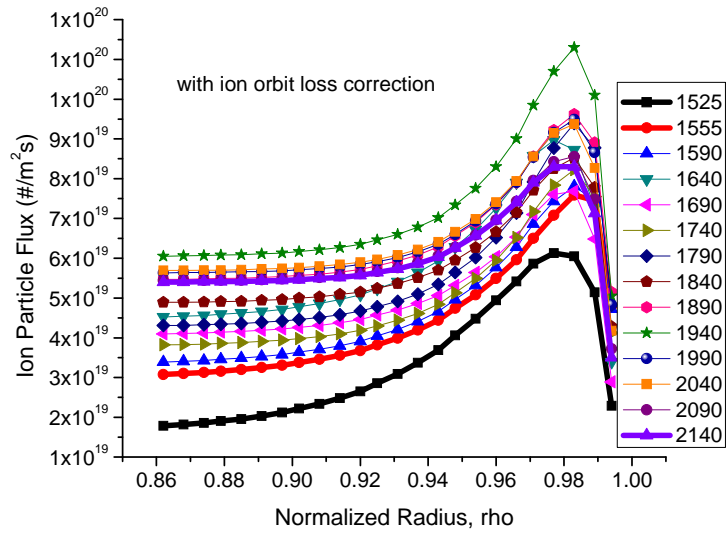
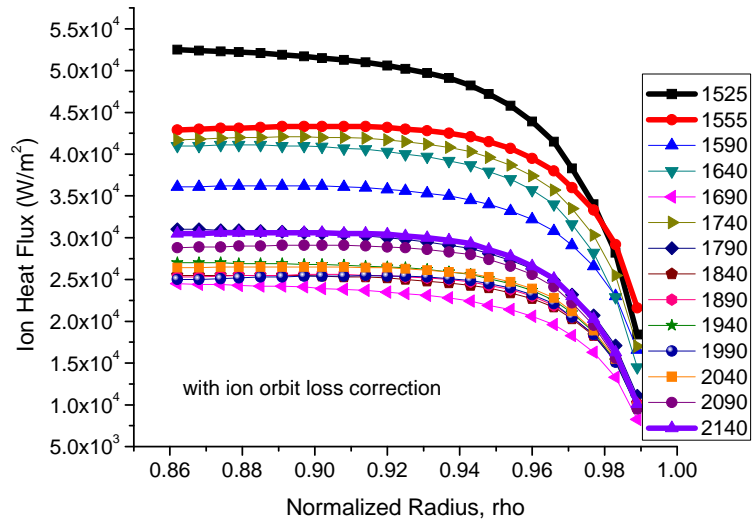FIGURE 18: Ion particle flux with ion orbit loss correction

FIGURE 19: Ion heat flux with ion orbit loss correction

4.2 Interpretation of particle transport

Particle transport is determined by momentum balance. The toroidal and radial components of the second velocity moment, or momentum balance, equation may be written for any ion species "j"

$$n_j m_j [(\nu_{jk} + \nu_{dj})V_{\phi j} - \nu_{jk}V_{\phi k}] = n_j e_j E_\phi^A + n_j e_j B_\theta V_{rj} + M_{\phi j} \tag{24}$$

and

$$V_{\phi j} = \frac{1}{B_\theta}\left[E_r + V_{\theta j}B_\phi - \frac{1}{n_j e_j}\frac{\partial p_j}{\partial r}\right] \tag{25}$$

where "k" in general refers to a sum over other ion species. In this paper "j" will refer to the main ion (deuterium) and "k" to the impurity ion (carbon) in a two-species model.

The quantity ν_{dj} is a toroidal angular momentum transfer frequency which represents the combined effect of viscosity, inertia, atomic physics, and other "anomalous" processes. Justification for representing the toroidal momentum transfer processes in this form is discussed in Ref. 33. $M_{\phi j}$ is the toroidal momentum input, e_j refers to the charge of species "j" and the other symbols have their usual meaning.

Subject to the assumption that there is a single impurity species "k" with the same logarithmic derivative and the same local temperature as the main ions "j", Eqs. 24 and 25 can be combined to arrive at a constraint on the main ion pressure gradient

$$-\frac{1}{p_j}\frac{\partial p_j}{\partial r} = \frac{V_{rj} - V_{rj}^{pinch}}{D_j} \tag{26}$$

where the "diffusion coefficient" is

$$D_j \equiv \frac{m_j T_j \nu_{jk}}{(e_j B_\theta)^2}\left(1 + \frac{\nu_{dj}}{\nu_{jk}} - \frac{e_j}{e_k}\right) \tag{27}$$

and the "pinch velocity"

$$V_{rj}^{pinch} \equiv \frac{\left[-M_{\phi j} - n_j e_j E_\phi^A + n_j m_j \left(\nu_{jk} + \nu_{dj}\right)\left(f_p^{-1}V_{\theta j} + E_r/B_\theta\right) - n_j m_j \nu_{jk}V_{\phi k}\right]}{n_j e_j B_\theta} \tag{28}$$

is a collection of normalized forces associated with the electric field, *VxB* forces and beam momentum input.

The fundamental transport coefficients that determine the main ion diffusion coefficient are the momentum exchange frequencies with impurities (ν_{jk}) and with neutrals (ν_{cx}), and the momentum exchange frequencies across flux surfaces due to viscosity and inertia, and any anomalous momentum exchange processes (the latter two are included in ν_{dj}).

If both the deuterium and carbon toroidal rotation velocities were measured, as is becoming possible, then Eqs. 24 for deuterium and carbon could just be solved for ν_{dj} and ν_{dk}, using the measured velocities as input. In the more common situation where only the ccarbon toroidal velocity is measured, it is necessary to resort to a perturbation analysis of Eqs. 24 for deuterium and carbon. Which lead[34,35].

$$\nu_{dj} = \frac{\left(n_j e_j E_\phi^A + e_j B_\theta \Gamma_j + M_{\phi j}\right) + \left(n_k e_k E_\phi^A + e_k B_\theta \Gamma_k + M_{\phi k}\right)}{\left(n_j m_j + n_k m_k\right) V_{\phi k}^{\exp}} \tag{29}$$

and for the carbon impurity ion

$$\nu_{dk} = \frac{\left(n_k e_k E_\phi^A + e_k B_\theta \Gamma_k + M_{\phi k}\right) + n_j m_j \nu_{jk} (V_{\phi j} - V_{\phi k})_0}{n_k m_k V_{\phi k}^{\exp}} \tag{30}$$

where

$$(V_{\phi j} - V_{\phi k})_0 = \frac{\left(n_j e_j E_\phi^A + e_j B_\theta \Gamma_j + M_{\phi j}\right) - n_j m_j \nu_{dj} V_{\phi k}^{\exp}}{n_j m_j \left(\nu_{jk} + \nu_{dj}\right)} \tag{31}$$

is the first order perturbation estimate of the difference in deuterium and carbon toroidal rotation velocities.

The momentum balance requirement of Eq. 26 can be rearranged into a form that clearly exhibits the diffusive and the non-diffusive components of the radial particle flux

$$\widehat{\Gamma}_j \equiv n_j V_{rj} = -\frac{n_j D_j}{p_j} \frac{\partial p_j}{\partial r} + n_j V_{rj}^{pinch} = -D_j \frac{\partial n_j}{\partial r} - D_j \frac{n_j}{T_j} \frac{\partial T_j}{\partial r} + n_j V_{rj}^{pinch} \tag{32}$$

The more general case when the assumption made above about the impurity distribution is not made is treated in Ref. 33.

The ion-impurity collision frequencies evaluated using the experimental densities and temperatures, the inferred experimental momentum transfer frequencies of Eq. 29 for deuterium and the resulting deuterium diffusion coefficient of Eq. 27 are displayed in Figs. 20 - 22.
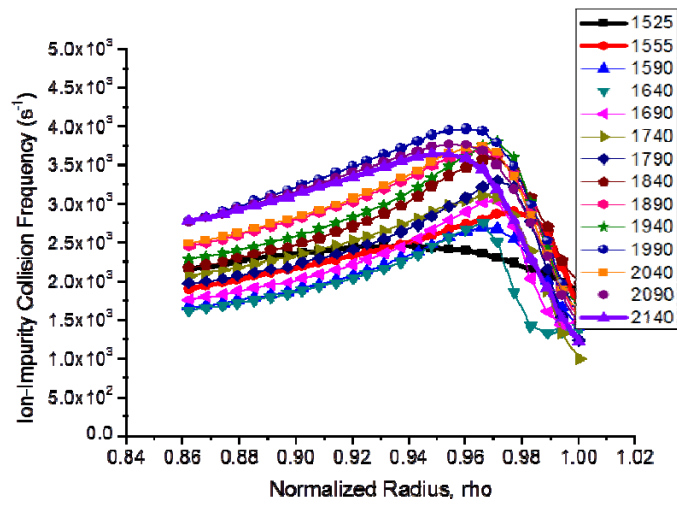

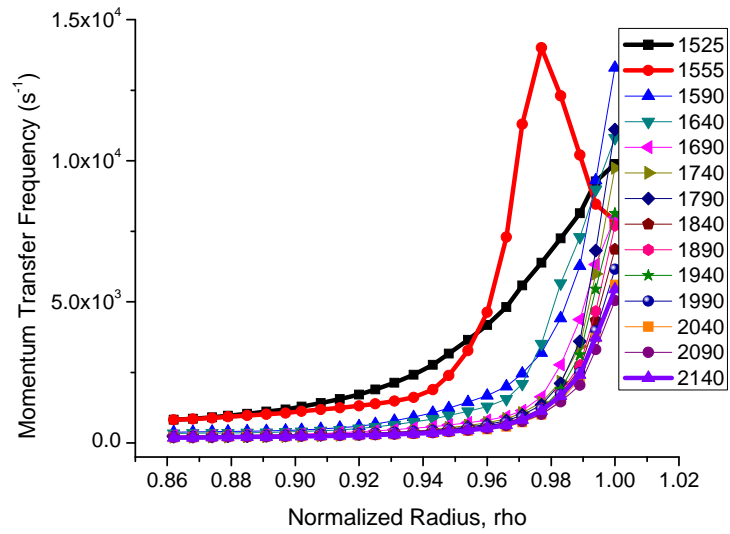FIGURE 20: Ion-Impurity collision frequencies

FIGURE 21: Toroidal momentum transfer frequencies

The abrupt increase in momentum transport frequency centered about $\rho = 0.98$ for the 1555 time is associated with the measured reduction in toroidal rotation in this region at that time, as shown in Fig. 7. This peaking in the momentum transfer frequency is directly reflected as a peak in the diffusion coefficient, as seen in Fig. 22.
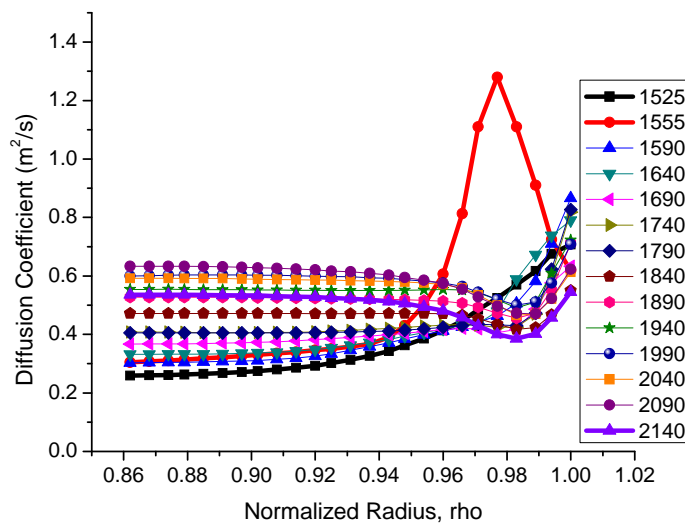

FIGURE 22: Diffusion Coefficients

The pinch velocity is slightly outward in L-mode, except just inside the separatrix, but a strongly inward pinch velocity develops over the region $\rho \geq 0.97$ immediately after the L-H transition (between 1525 and 1555 ms), as shown in Fig. 23. The various component of the pinch velocity expression of Eq. 28 are plotted separately in Fig. 24. In L-mode (1525 ms), the E_r and V_θ components are oppositely directed and almost cancel, leaving a small pinch velocity. Immediately after the L-H transition (1555 ms) the E_r component becomes strongly inward, reflecting the strong negative value of the radial electric field just after the L-H transition, and these two dominant components reinforce each other to produce a strongly inward pinch velocity. At later times the E_r and V_θ components becomes less strongly inward, as does the net pinch velocity.
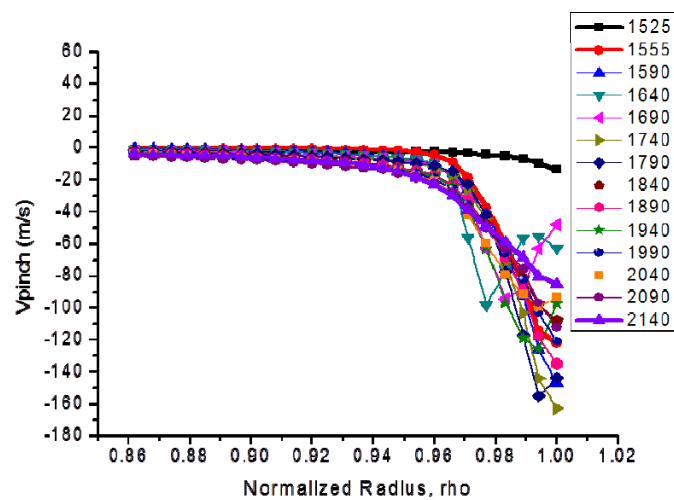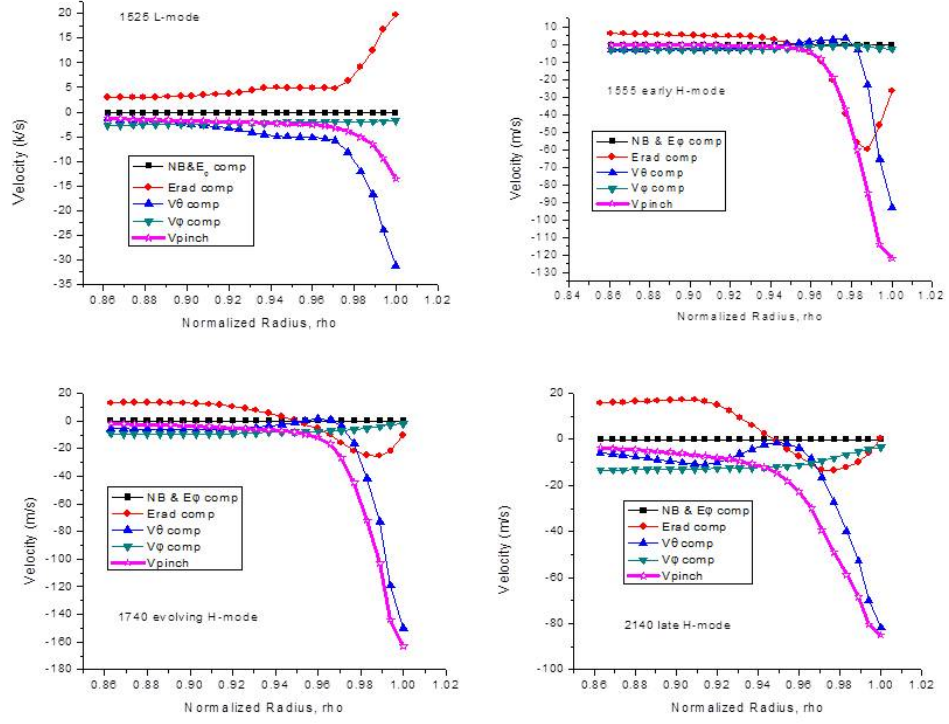

FIGURE 23: Pinch Velocity

FIGURE 24: Components of the pinch velocity for selected time

4.3 Thermal conduction

The heat conduction relation

$$q_{j,e} = -n_{j,e}\chi_{j,e}\frac{\partial T_{j,e}}{\partial r} \tag{33}$$

is used to determine the thermal diffusivity from the experimental temperature profiles

$$\chi_{j,e}^{\exp} = -\frac{q_{j,e}^{\exp}}{n_{j,e}^{\exp}\left(\partial T_{j,e}^{\exp}/\partial r\right)} = -\frac{\left(Q_{j,e}^{\exp} - 1.5\Gamma_{j,e}^{\exp}T_{j,e}^{\exp}\right)}{n_{j,e}^{\exp}\left(\partial T_{j,e}^{\exp}/\partial r\right)} \tag{34}$$

where $Q_{j,e}^{\exp}$ is obtained by solving Eq. 15 or 16 for the total heat flux (and correcting for

ion orbit loss for the ions) , and $\Gamma_{j}^{\exp}$ is obtained by solving Eq. 14 for the total radial

33

particle flux (and correcting for ion orbit loss) and Γ_e^{exp} is constructed there from taking into account impurities.

The electron thermal diffusivity decrease immediately after the L-H transition (between 1525 and 1555 ms) and generally continues to decrease as the H-mode evolves, forming a "well" or "transport barrier" that moves inward with time following the L-H transition.
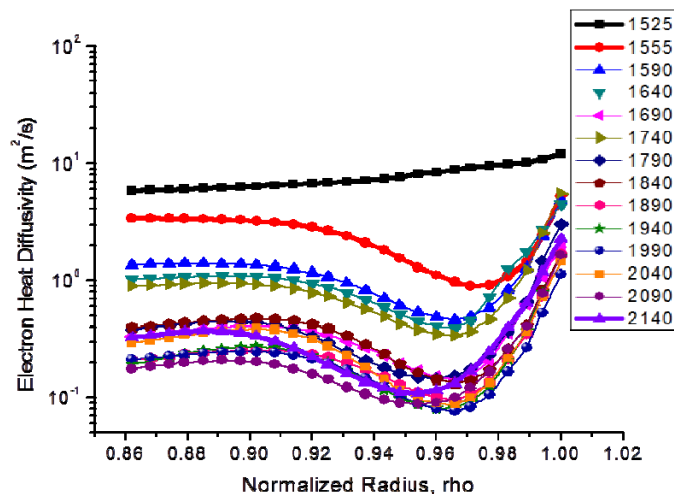
FIGURE 25: Experimental electron thermal diffusivity

The ion thermal diffusivity also decreases at the L-H transition and continues to decrease as the H-mode evolves, as shown in Fig. 26 and 27, but does not seem to form the "well" or "transport barrier" structure seen for the electron thermal diffusivity. The strong effect upon the interpreted ion thermal diffusivity just inside the separatrix of the ion orbit loss correction can be seen by comparing Figs. 26 and 27.

FIGURE 26: Experimental ion thermal diffusivity with ion orbit loss correction.

FIGURE 27: Experimental ion thermal diffusivity without ion orbit loss correction.

CHAPTER 4

SUMMARY AND CONCLUSION

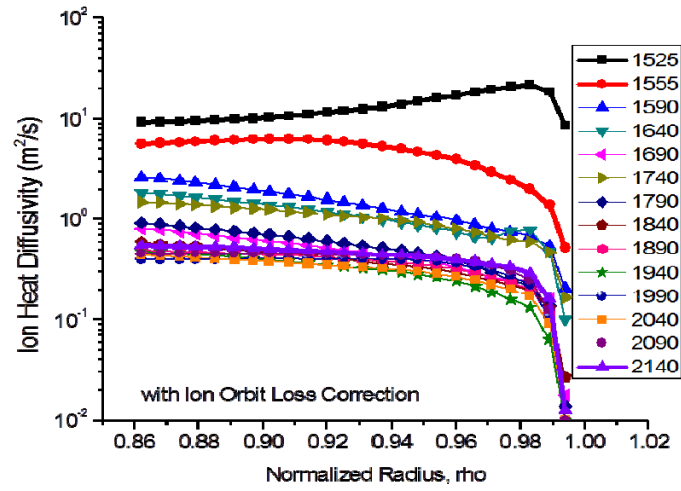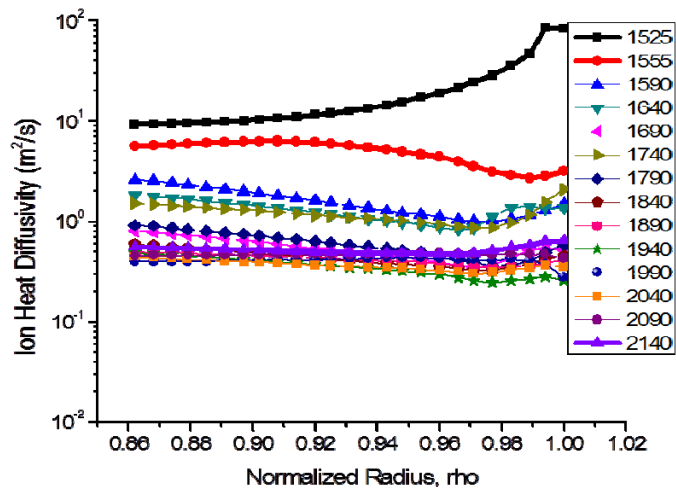The evolution of diffusive and non-diffusive transport during a L-H transition has been interpreted from a force-balance analysis of the measured density, temperature and rotation velocities in the plasma edge of a DIII-D discharge.

Observation of experimentally obtained density, temperature and rotational velocity profiles indicate large changes in plasma behavior early in transition. Close examination of measured parameters indicate that most significant changes occur when the plasma transitons from L-mode (1525ms) to early (transitional) H-mode (1555-1590ms). While the most significant changes occur in first 30-70ms into the transition, the measured profiles continue to evolve, non-monotonically, over another several hundred milliseconds.

Momentum balance requires that the radial particle flux satisfies a "pinch-diffusion" relations and defines the values of the diffusion coefficient and the pinch velocity in terms of quantities that can be determined from experiment. The deuterium diffusion coefficient can be determined from measured quantities: the ion-impurity collision frequency, which can be determined from the measured densities and temperatures; and the momentum transport frequency, which can be inferred from the measured toroidal rotation velocities. The unmeasured Deuterium rotational velocity profile and the Deuterium and Carbon momentum transport frequencies are determined from the measured Carbon toroidal rotation velocity by using first order perturbation theory.

The measured Carbon toroidal rotation velocity and the Deuterium toroidal rotational velocity calculated from it are observed to decrease in the outer plasma edge immediately following the L-H transition, whereas they increase immediately after the L-

H transition for $\rho < 0.95$. This causes an increase in the interpreted momentum transport frequencies for $\rho > 0.95$, which produces a sharp peaking in the interpreted Deuterium diffusion coefficient immediately after the L-H transition. This structure for $\rho > 0.95$ gradually disappears from the measured rotation velocity and the interpreted diffusion coefficient profiles at later times. The overall effect is a transition from a diffusion coefficient profile in L-mode that increases sharply with radius for $\rho > 0.95$ to a fully developed H-mode diffusion coefficient profile in which the H-mode value is about twice the L-mode value for $\rho < 0.95$, but for which there is a pronounced reduction relative to L-mode and a 'transport barrier' well-like structure of the diffusion coefficient for $\rho > 0.95$.

The pinch velocity is a collection of normalized electromagnetic forces specified by momentum balance requirements in which there are terms proportional to the toroidal and poloidal rotation velocities, a term proportional to the radial electric field, and (smaller) terms proportional to external momentum torques and the induced toroidal electric field. In this discharge, the radial electric field and the poloidal velocity terms were dominant. The radial electric field, which was calculated from the radial momentum balance using measured Carbon density, temperature and rotation velocities, changed dramatically from the small, positive and relatively flat L-mode profile to a profile which increased to positive values an order of magnitude larger (10-20 kV) for $\rho < 0.95$ but became strongly negative for $\rho > 0.95$ (-10-20kV) immediately following the L-H transition. The Deuterium poloidal rotation velocity also changed dramatically from the small, positive and relatively flat L-mode profile (calculated from the Deuterium radial momentum balance) to a H-mode profile strongly peaked (20-30 km/s) for $\rho > 0.95$. The net effect of these two dominant terms was to produce a dramatic change

in the small $\left(\sim 10 m/s\right)$ inward pinch velocity in the outer region of the L-mode edge plasma to a large $\left(\sim 100 m/s\right)$ inward pinch velocity in H-mode.

Thus, immediately following the L-H transition, there is a factor of ~ 10 increase in the inward particle pinch velocity and a factor ~ 2 decrease in the particle diffusion coefficient.

Electron and ion thermal/heat diffusivity profiles also exhibit significant change in magnitude as plasma enters transition phase. Initially, both diffusivity profiles are relatively flat across the edge region in L-mode. Sharp decrease in both electron and ion diffusivity profiles are observed in early transition (1555ms). Such reduction in diffusivity is an indication of i) particle and energy confinement improvements and ii) development of transport barrier. Non-monotonic changes in thermal diffusivity profiles are observed after significant change occurs.

Calculation of ion-orbit loss effects across the edge region indicates steady increase in both particle and energy loss fractions as a function of time as plasma enters H-mode confinement. Results of ion and energy loss fraction are entered into ion heat diffusivity calculation to account for its effect. While resulting profiles indicate similar conclusion where the heat diffusivity decreases drastically from 1525ms to 1590ms, inclusion of ion-orbit loss effect cause a drastic drop in thermal diffusivity at the edge of plasma.

Based on obtained results, a conclusion can be drawn that majority of edge pedestal development occurs early in confinement mode transition. All parameters exhibit a substantial change between 1525 (L-mode) and 1555 (early transition) ms and a further significant change between 1555 and 1590 ms. As plasma enters further into the transition and H-mode, rather small and non-monotonic changes in profiles take place. In order to obtain detailed plasma behavior, more highly time-resolved data over the first 50-100 ms after the L-H transition should be obtained. Future investigation should

include examination of various discharges that undergo confinement mode transition to establish a plasma behavior model. Determination of plasma behavior model will enable development of transient predictive model to predict plasma behavior through confinement mode transition.

REFERENCES

[1]   *Q: Are all atoms radioactive*. 3/13/11. Retrieved October 9, 2012 From
      www.askamathematician.com/2011/03/q-are-all-atoms-radioactive/

[2]   PRUSSIN, S. G. *Nuclear Physics for Applications: a Model Approach.* Weinheim:
      Wiley-VCH (2007).

[3]   STACEY, W. M. *Fusion Plasma Physics*. Weinheim: Wiley-VCH (2005).

[4]   *Nuclear fusion 4.7.7.* Retrieved October 10, 2012 From
      www.kayelaby.npl.co.uk/atomic_and_nuclear_physics/4_7/4_7_4.html.

[5]   Lockheed Martin. *Nuclides and Isotopes: Chart of Nuclides* (16th ed.). E. M. Baum,
      H. D. Knox, and T. R. Miller (Ed.). Schenectady, NY: Knolls Atomic Power
      Laboratory, Inc. (2002).

[6]   STACEY, W. M. *Fusion* (1st ed.). Weinheim: Wiley-VCH (1984).

[7]   *ITER- the way to new energy*. Retrieved October 9, 2012 From
      www.iter.org/mach/magnets.

[8]   *Nuclear Fusion, Fusion Reactors*. www.splung.com/content/sid/5/page/fusion
      (accessed October 9, 2012)

[9]   F. Wagner, G. Becker, K. Behringer, D. Campbell, A. Eberhagen, W. Engelhardt, G.
      Fussmann, O. Gehre, J. Gernhardt, G. V. Gierke, G. Hass, M. Huang, F. Karger, M.
      Kielhacker, O. Kluber, M. Dornherr, K. Lackner, G. Lisitano, G. G. Lister, H. M.
      Mayer, D. Meisel, F. R. Muller, H. Murmann, H. Niedermeyer, W. Poschenrieder, H.
      Rapp, H. Rohr, F. Scheider, G. Siller, E. Speth, A. Stabler, K. H. Steur, G. Venus, O.
      Vollmer and Z. Yu, Phys. Rev. Lett. 49, 1408 (1982).

[10] R. J. Groebner, K. H. Burrell and S. P. Seraydarian, Phys. Rev. Lett. 64, 3015 (1990).

[11] C. F. Maggi, Nucl. Fusion 50, 066001 (2010).

[12] W. M. Stacey and R. J. Groebner, Phys. Plasmas 17, 112512 (2010).

[13] M. Kotschenreuther, W. Dorland, Q. P. Liu, et al., Proc. 16th Conf. Plasma Phys Controlled Fusion Research, Montreal 1996 (IAEA, Vienna, 1997) Vol. 2, p 371.

[14] J. E. Kinsey, R. E. Waltz and D. P. Schissel, Proc. 24th Euro. Phys. Soc. Berchtesgarten, 1997, Vol. , p 1081.

[15] K. H. Burrell, Phys. Plasmas 4, 1499 (1997).

[16] P. W. Terry, Rev. Mod. Phys. 72, 109 (2000).

[17] M. A. Mahdavi, R. Maingi, R. J. Groebner, A. W. Leonard, T. H. Osborne and G. D. Porter, Phys. Plasmas 10, 3984 (2003).

[18] P. B. Snyder, R. J. Groebner, T. H. Osborne and H. R. Wilson, Phys. Plasmas 16, 056118 (2009).

[19] W. M. Stacey, R. J. Groebner and T. E. Evans, "Non-diffusive transport in the tokamak edge pedestal", Nucl. Fusion, to be published (2012).

[20] J. Luxon, Nucl. Fusion 42, 614 (2002).

[21] W. M. Stacey and R. J. Groebner, Phys. Plasmas 17, 112512 (2010).

[22] W. M. Stacey and R. J. Groebner, Phys. Plasmas 14, 012501 (2007).

[23] P. Gohil, K. H. Burrell, R. J. Groebner, and R. P. Seraydarian, Rev. Sci. Instrum 61, 2949 (1990).

[24] T.N. Carlstrom, G.L. Campbell, J.C. DeBoo, R. Evanko, J. Evans, C.M. Greenfield, J. Haskovec, C.L. Hsieh, E. McKee, R.T. Snider, R. Stockdale, P.K. Trost, and M.P. Thomas, Rev. Sci. Instrum. 63, 4901 (1992).

[25] T.N. Carlstrom, C.L. Hsieh, R.Stockdale, D.G. Nilson and D.N. Hill, Rev. Sci. Instrum. 68, 1195 (1997).

[26] P. Gohil, K.H. Burrell, R.J. Groebner, J. Kim, W.C. Martin, E.L. McKee, and R.P. Seraydarian, 1991 Proc. 14th Symp. in Fusion Engineering (San Diego, CA) vol 2 (New York: Institute of Electrical and Electronics Engineers) p 1199.

[27] T.N. Carlstrom, K.H. Burrell, R.J. Groebner, A.W. Leonard, T.H. Osborne and D.M. Thomas, Nucl Fusion 39, 1941 (1999).

[28] P.Gohil, K.H. Burrell, E.J. Doyle, R.J. Groebner, J. Kim, R.P. Seraydarian, Nucl. Fusion 34, 1057, (1994).

[29] W.M. Stacey, Phys. Plasma 5,1015 (1998).

[30] W.M. Stacey, Phys. Plasma 8, 3673 (2001).

[31] W.M. Stacey, Nucl. Fusion, 40, 965 (2000).

[32] W.M. Stacey, Phys. Plasma 18,102504 (2011).

[33] W. M. Stacey, Contrib. Plasma Phys 48, 94 (2008).

[34] F. Castejón, S. Eguilior, I. Calvo, D. López-Bruna, and J. M. García-Regaña, Phys. Plasma 15, 012504 (2008).

[35] W.M. Stacey and R.J. Groebner, Phys. Plasma 16, 102504 (2009).